

Adaptive Control of Undetected Radio Frequency Interference With a Spaceborne Microwave Radiometer

David D. Chen, *Graduate Student Member, IEEE*, and Christopher S. Ruf, *Fellow, IEEE*

Abstract—In microwave radiometric remote sensing, undetected radio frequency interference (RFI) can adversely affect the accuracy of the science products. A method is presented to adaptively tune the parameters of an RFI detection algorithm which controls the equivalent brightness temperature of undetected RFI. The method is adaptive in the sense that it adjusts to variations in the RFI environment, e.g., from high RFI conditions near some population centers to low RFI conditions in the tropical Pacific Ocean. The RFI environment is characterized by inferring the distribution of low-level undetected RFI from that of high-level detected RFI using appropriate scaling arguments. The resulting tuned algorithm adjusts its detection threshold to equalize the brightness temperature calibration bias due to RFI at the expense of the now variable measurement precision (noise equivalent delta temperature). This tradeoff between calibration bias and measurement precision can be represented as a modified version of the classic receiver-operating-characteristic curve. The radiometer on the Aquarius/SAC-D mission is used as an example.

Index Terms—Microwave radiometry, radio frequency interference (RFI), remote sensing.

I. INTRODUCTION

A. RFI in Spaceborne Radiometry

SINCE the 1960s, spaceborne microwave radiometry has played a major role in the remote sensing of the Earth and other planets. With the proper selection of different frequencies, polarizations, and incidence angles, many useful land, oceanic, cryospheric, and atmospheric parameters can be determined from the measured thermal emission. In the case of Earth observations, two of these physical parameters are sea-surface salinity (SSS) and soil moisture (SM). SSS affects the formation of water masses, controls 3-D ocean circulation, and plays a significant role in climate studies [1]. SM is a key parameter in many hydrological, agricultural, and meteorological applications, including numerical weather prediction models [2].

Although the science of passive microwave remote sensing has made significant progress in recent decades, one of the most critical issues faced by microwave radiometers today is

Manuscript received November 25, 2014; revised February 23, 2015; accepted March 11, 2015.

D. D. Chen is with the Electrical Engineering and Computer Science, University of Michigan, Ann Arbor, MI 48109-2122 USA.

C. S. Ruf is with the Atmospheric, Oceanic, and Space Sciences, University of Michigan, Ann Arbor, MI 48109-2143 USA.

Color versions of one or more of the figures in this paper are available online at <http://ieeexplore.ieee.org>.

Digital Object Identifier 10.1109/TGRS.2015.2414395

TABLE I
AQUARIUS RADIOMETER INSTRUMENT CHARACTERISTICS

	Beam 1	Beam 2	Beam 3
Incidence Angle (degrees)	28.7	37.8	45.6
3dB Footprint Size (km)	94 x 76	120 x 84	156 x 97
3dB Beam Width (degrees)	6.1	6.3	6.6

that of radio frequency interference (RFI). Despite the fact that spaceborne microwave radiometers generally operate within protected or shared spectral bands that are designated for scientific research, previous experience with research satellites (e.g., SMOS, SSM/I, AMSR-E, and WindSat) [3]–[5] and airborne campaigns [6], [7] have indicated that the RFI that radiometers are subjected to can be significant. Since radiometers are required to measure very low levels of electromagnetic radiation with a high degree of precision and accuracy, even very small biases in the observations due to RFI can put the science objectives of a mission at risk. For instance, the Aquarius mission is dedicated to the measurement of global SSS, and it requires a calibration accuracy for brightness temperature of about 0.1 K at average sea surface temperature and salinity values to achieve an accuracy in SSS of 0.2 psu [8]. The severity of RFI has led to the design of novel radiometer instrumentation and signal processing [9], [10] and has influenced key radiometer design parameters such as integration time.

B. Aquarius RFI Detection and Mitigation

The Aquarius satellite was launched in June 2011 and includes a microwave radiometer operating at 1.4 GHz to measure SSS. The Aquarius instrument has three antenna beams generated by individual antenna horns each with its own dedicated radiometer which all operate in parallel [11]. Their approximate incidence angles and footprint sizes are given in Table I [1].

The shortest antenna observation, known as a short accumulation sample, has an integration time of about 10 ms. This is much shorter than that required to achieve the Nyquist spatial sampling rate and is designed to enhance Aquarius' ability to detect and mitigate pulsed RFI [12]. The Aquarius ground-processing software produces antenna temperature products at 1.44-s intervals. Two antenna temperature products are available: The "TA" product bypasses the RFI detection and mitigation algorithm altogether and averages all available observations in the 1.44-s interval. The "TF" applies an RFI detection algorithm designed to flag and remove RFI-contaminated

samples and averages the remaining samples in the 1.44-s interval. TA is primarily used for evaluation purposes, while TF is used downstream to produce science products such as salinity.

The Aquarius RFI detection algorithm is a time-domain “glitch” detector. Individual samples under test (SUTs) are compared to the average of surrounding samples and are flagged as containing RFI if the difference between an SUT and its surrounding average value exceeds a specified threshold (see Appendix A for a summary and [12] for details). The Aquarius RFI detection threshold is primarily dictated by the brightness temperature detection parameter, TD. The parameter specifies the allowable difference between a SUT and its surrounding average, above which RFI is assumed to be present. TD is currently specified in units of the standard deviation of the additive noise that is present in each sample. The noise is modeled as a zero mean Gaussian. Its standard deviation is commonly referred to in microwave radiometry as the noise equivalent delta temperature (NEDT). In an RFI-free environment, the false alarm rate (FAR) of the RFI detection algorithm is readily determined from the value of TD. False alarms occur when RFI is not present but the additive noise in a SUT deviates sufficiently from the average noise of surrounding samples. If, for example, a TD value of 3 were used, false alarms would occur whenever a realization of the noise exceeded three times its standard deviation. The resulting FAR of the Aquarius RFI algorithm is found, using a Monte Carlo simulation of the implemented algorithm, to be approximately 4.0%. A Monte Carlo approach is used, rather than simply integrating a truncated Gaussian probability distribution, in order to account for the effects of numerous algorithm implementation details, including the iterative way that outliers are removed and the fact that additional samples near ones with detected RFI are also flagged as a conservative safety precaution. The truncated Gaussian, or error function, approach is found to significantly underestimate the true FAR.

The impact of false alarms on Aquarius’ science data products is to reduce the number of individual 10-ms samples that are averaged together into the 1.44-s products. This, in turn, raises the NEDT of the 1.44-s products. For example, given a TD of 3, the NEDT of a 1.44-s science data product would be increased by about 2.3%.

In addition to the FAR, the TD threshold also determines the sensitivity of the detection algorithm to RFI. The higher the TD is, the stronger the RFI must be in order to be detected.

C. ROC Curve

The performance of an RFI detection and mitigation system is characterized by statistics related to the FAR and to the probability of detection (PD). The FAR is the probability that an uncontaminated sample will be flagged as RFI. The PD is the probability that a contaminated sample will be flagged as RFI. The FAR and the PD are competing statistics. By adjusting the detection threshold of an RFI algorithm, one can trade off one statistic against the other. This relationship is depicted graphically by the receiver operating characteristic (ROC) curve [13]. In Fig. 1, a particular value for the detection threshold is shown, with the resulting FAR and PD statistics illustrated. The two

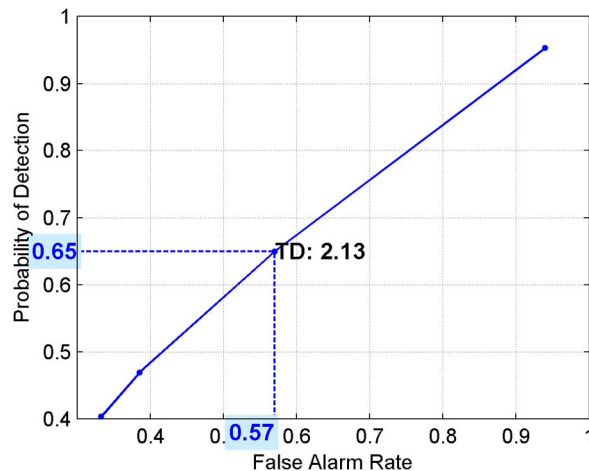


Fig. 1. Example of an ROC curve for Aquarius, and the resulting FAR and PD that are produced by a particular setting of the detection threshold parameter, TD, in the RFI detection algorithm. FAR equals the number of uncontaminated samples flagged with RFI divided by the total number of uncontaminated samples. PD equals the number of contaminated samples flagged with RFI divided by the total number of contaminated samples. The estimation of these statistics requires knowledge of the RFI environment, which is derived using the method described in Section III. The RFI environment is found to depend strongly on location. The example shown here is for the grid box centered at 59.5 N and 26 W and is derived from radiometer measurements by Beam 1, H-Pol, and ascending node.

detection statistics have been computed assuming a particular RFI environment, at a particular location in the North Atlantic, and derived from measurements by the Aquarius radiometer over a particular period of time. The RFI environment is characterized by a probability distribution of its amplitude, which is computed using an extension of the method developed in [14]. Details of the method and how it was extended are provided in Section III. The selected detection threshold is referred to as the “operating point” on the ROC curve.

The PD statistic always depends on the RFI environment. In the case of the Aquarius RFI detection algorithm, the environment also affects the FAR statistic. This results from the conservative approach taken by the algorithm, in which, whenever RFI is detected in a sample, its neighboring samples are also flagged with RFI even if none was detected there. As a result, more false alarms will occur in environments with a high likelihood of RFI. This is illustrated in Fig. 1 by a ROC curve that was derived in a particularly “RFI-rich” region of the North Atlantic. The high FAR of 57% noted for a detection threshold set to 2.13 σ is a direct result of this aspect of the algorithm.

The RFI environment has been found to vary strongly with location and orbit node (ascending or descending) for the Aquarius mission [15]. The Aquarius mission currently uses an RFI detection threshold which is set to equalize the FAR in an RFI-free environment. It is important to note that this can result in significant variations in the PD of the RFI and, hence, in the calibration bias that is present in the brightness temperature measurements, as a function of location and orbit node.

II. OBJECTIVES AND OUTLINE

Since the NEDT of individual brightness temperature measurements is not a driving source of error in the Aquarius

salinity measurements, it is not an optimal cost function by which to set the operating point on the ROC curve. One driving source of error is the calibration bias in the brightness temperature measurements, one component of which is the contribution by undetected RFI. We introduce here a new cost function, the expected value of the equivalent brightness temperature of undetected RFI, denoted as $\langle TB_{RFI} \rangle$. It is examined in detail hereinafter. In terms of its impact on the scientific value of Aquarius salinity measurements, $\langle TB_{RFI} \rangle$ is a more relevant cost function to control by tuning the RFI algorithm (i.e., by setting the operating point on the ROC curve). To that end, we introduce in Section V a modified form of the ROC curve which has $\langle TB_{RFI} \rangle$ on the y -axis and NEDT on the x -axis.

Peak hold RFI maps, shown in Fig. 2, are a way to illustrate the global RFI environment. They are constructed by taking the maximum TA observed (over some time interval) and subtracting from it a location-dependent TB climatology (derived from an average value of RFI-free measurements) [15]. In the figure, the strength of the RFI is reported as its “equivalent brightness temperature” to indicate how bright the thermal emission would need to have been to produce the same detected power level. Since RFI typically originates from point sources whereas thermal emission is produced by extended sources that fill a radiometer’s antenna beam, the equivalent brightness temperature produced by RFI will be instrument dependent.

The peak hold maps shown here demonstrate that the RFI environment is strongly dependent on location and orbit node. It may also differ with polarization. For this reason, the level of undetected RFI will also vary. The objective of this work is to tune the detection threshold of the RFI algorithm in response to the local RFI environment so that $\langle TB_{RFI} \rangle$ has a constant (acceptably low) value. Different threshold values should, in principle, be set at each operating condition (location, orbit node, and polarization). To demonstrate our tuning method, we focus in this paper on the horizontal polarization and ascending node of Beam 1 of the Aquarius radiometer. However, the method is general and could be applied to other instruments and RFI algorithms as well.

A. Overview of the Tuning Process

In order to estimate $\langle TB_{RFI} \rangle$, it is necessary to characterize the RFI environment. We do so at each location statistically, using an archive of past detected RFI. A location-dependent probability distribution is derived for the magnitude of RFI. Next, $\langle TB_{RFI} \rangle$ is estimated at each location as a function of the TD threshold setting of the RFI algorithm using a Monte Carlo-type simulation seeded by the RFI probability distribution. The procedural steps followed to perform this analysis are as follows:

Step 1) Model the signal observed by Aquarius as the sum of the net thermal emission (i.e., planetary brightness temperature plus receiver noise temperature) and the equivalent RFI brightness temperature, as given by

$$TA_{total}(t) = TA_{sys}(t) + TA_{RFI}(t) \quad (1)$$

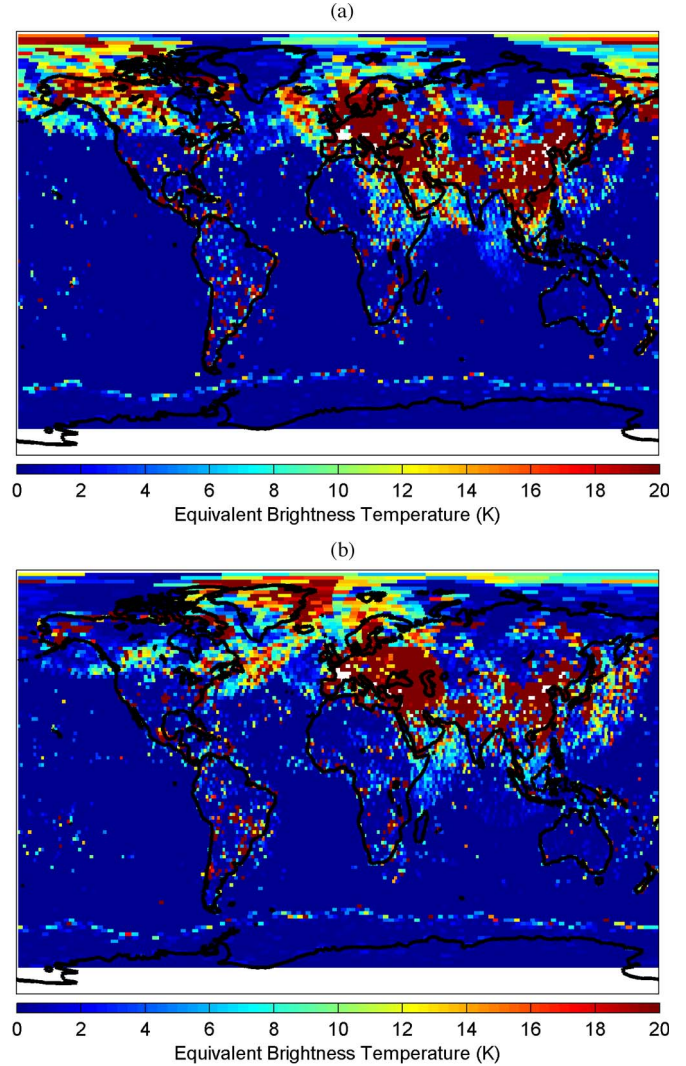


Fig. 2. RFI peak hold maps for the (a) ascending and (b) descending orbit nodes, based on Aquarius radiometer measurements made over the period from August 25, 2011 to January 1, 2012. Note that, at each location, the map indicates the peak RFI TB level as seen by the radiometer when the antenna boresight points at that location. The actual RFI source may not originate at the said location and may instead enter the radiometer through the antenna sidelobes.

$TA_{sys}(t)$ is modeled as a Gaussian distributed random variable. Its mean is assumed to be 398 K and is typical of measurements made by Aquarius over the open ocean (see Appendix B for its derivation). The standard deviation is assumed to be 0.8 K for a 10-ms integration time and is a typical value for the NEDT of the Aquarius measurements over the open ocean (see Appendix C for its derivation). Modeling of the probability distribution of $TA_{RFI}(t)$ is treated in Section III.

Step 2) Generate a sequence of random $TA_{total}(t)$ with $TA_{RFI}(t)$ set to zero, and use only the distribution of $TA_{sys}(t)$. Process this sequence with the Aquarius ground-processing software, with the RFI detection and mitigation algorithm bypassed, to obtain a sequence of 1.44-s TAs. These are the desired TAs without RFI corruption. Denote this sequence by TA1.

- Step 3) This step resembles Step 2), except that RFI is now added to generate a sequence of $TA_{total}(t)$. In addition, we now invoke the RFI algorithm in ground processing to obtain 1.44-s TFs. Denote this sequence by TF2.
- Step 4) By subtracting each value of TA1 from the corresponding value of TF2 and taking the mean of the resulting difference sequence, we arrive at $\langle TB_{RFI} \rangle$.
- Step 5) The corresponding NEDT of the 1.44-s data products is derived. We derive this NEDT in an RFI-free environment, in order to estimate the NEDT that is present most of the time. In practice, the NEDT is generally increased when RFI is present due to the mitigation stage of the RFI algorithm, which reduces the number of samples used in the 1.44-s integration. A Monte Carlo approach is used and is discussed in more detail in Section IV-D.

By varying TD in the RFI algorithm in Step 3), $\langle TB_{RFI} \rangle$ and NEDT can be determined for each TD setting, and the modified ROC curve can then be constructed for the particular location under consideration. The operating point on the ROC curve (and thus the TD setting) can then be determined, given the desired level of $\langle TB_{RFI} \rangle$. The same procedure can be applied to other operating conditions (location, orbit node, and polarization) to complete the tuning process.

We begin with an examination of $TA_{RFI}(t)$ in the next section.

III. MODELING THE PROBABILITY DISTRIBUTION OF RFI

For RFI power levels with equivalent brightness temperatures near or below the NEDT level, reliable detection can be very problematic. However, at higher levels, the RFI is typically straightforward to detect. Under the assumption of stationarity over time, but variability in space, low-level undetected RFI that enters the antenna pattern through its sidelobes can be estimated by considering the appropriate neighboring location at which it entered the main beam of the antenna at a much higher, and thus detectable, signal strength. Conversely, if we assume that the detected RFI is omnidirectional, the detected RFI also enters the sidelobes in other neighboring locations, but at a lower signal strength. The ratio of detected (main beam entrant) signal strength to undetected (sidelobe entrant) signal strength will depend on the sidelobe level of the antenna pattern in the appropriate direction as well as on the propagation range.

A process to estimate the distribution of RFI is described in [14], and that process is augmented here (with the inclusion of land-based RFI for instance), resulting in RFI distributions that are more accurate and complete. We consider three representative locations, shown in Fig. 3, to demonstrate our method. Iceland is subjected to strong RFI in both ascending and descending orbit nodes. U.K. receives strong RFI in ascending but not descending passes. Tropics experiences little RFI overall.

A. Detected RFI

To characterize the RFI environment, we compute the difference between a “TB climatology” and measurements that

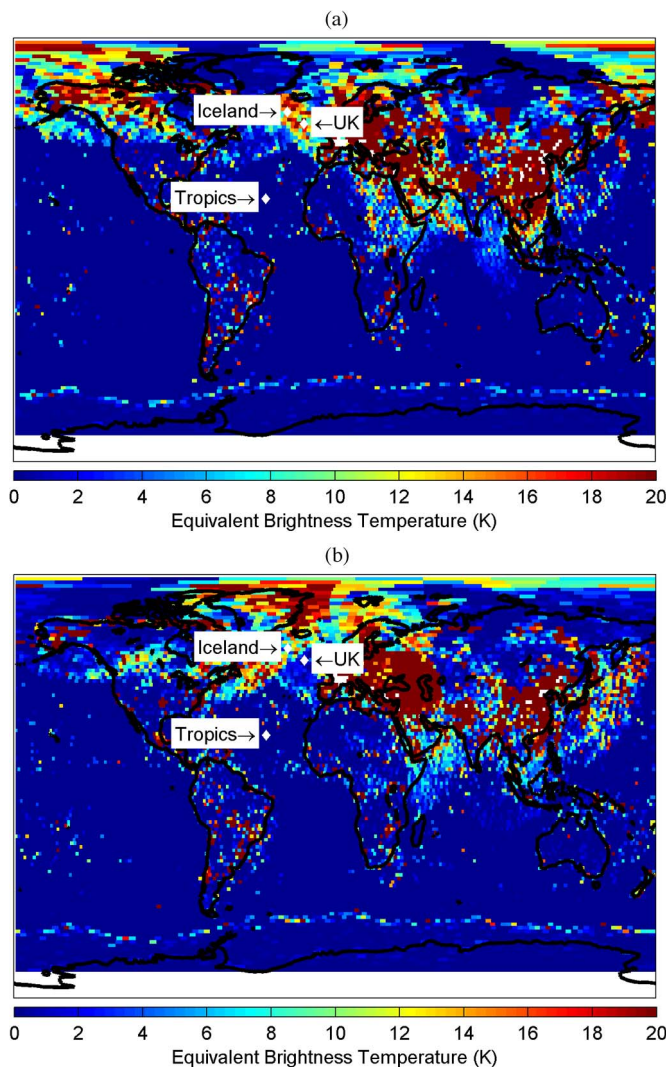


Fig. 3. Three representative locations of peak RFI TB for characterization of the RFI environment on (a) ascending and (b) descending orbit nodes. They are 59.50 N 26.00 W (referred to as Iceland), 54.27 N 16.88 W (referred to as U.K.), and 22.43 N 38.32 W (referred to as Tropics).

have no RFI mitigation performed. The TB climatology is a location-dependent estimate of what the TB would have been if no RFI had been present. It is derived using a three-stage process. In most cases, with only low level or occasional RFI, the “clean mean” estimate of TB at a location is used. (See Appendix A for a description of the Aquarius RFI detection algorithm, which includes the calculation of the clean mean.) In some cases, undetected RFI can bias the clean mean to the point where it is higher than the physical surface temperature at that location. At those locations, the physical temperature is used instead, as a conservative upper bound on the TB climatology. At locations where RFI is extremely persistent, a clean mean may not be able to be computed at all. In those cases, a zonal average of clean means at similar latitudes is used.

The clean mean may be biased by RFI—this can happen if the RFI has a high duty cycle for instance. Since the natural TB is always less than the physical surface temperature, a simple attempt at removing this bias is to use the minimum of some physical surface temperature climatology data and our clean mean

TB climatology. The ancillary data product used is the NCEP Climate Forecast System Reanalysis monthly mean [16], [17].

The estimated magnitude of the detected RFI does not need to be especially accurate for our purposes. The detected RFI is used to estimate the undetected RFI in neighboring locations which enter the data through the antenna sidelobes. As such, its magnitude is attenuated by the relative sidelobe level of the antenna at that location, and the RFI levels are correspondingly reduced. In addition, the detected RFI is also directly included in the RFI PDF for the location at which it is collected. Because these RFI are high enough to be detected and mitigated, they do not contribute significantly to $\langle TB_{\text{RFI}} \rangle$. In the event that the climatology at a particular location cannot be derived due to a lack of clean mean data, it is estimated by zonally averaging the climatology of other locations at the same latitude and with a similar antenna gain-weighted land fraction present. Similar latitudes are used to reflect the general dependence of SSS and temperature, and hence of TB, on latitude. Similar land fractions are used to reflect the bias in ocean TBs introduced by land in the antenna sidelobes.

The detected RFI is estimated by subtracting the samples flagged with RFI from the climatology. Those samples not flagged are assigned a value of 0 for detected RFI, even though these samples may indeed contain undetected RFI. The undetected RFI is taken into account at a later step. There are occasionally samples containing sufficiently high RFI levels which result in a power level above the dynamic range of the Aquarius instrument. When a sample is affected by these high-power RFI, the instrument sets an overflow flag, and we assign a conservative value of 3000 K to the detected RFI, as 3000 K has been found empirically to be approximately the upper limit of the instrument dynamic range.

Once a population of detected RFI has been assembled at a particular location, the corresponding RFI distribution can be derived. Examples of the RFI distributions are shown in Fig. 4 for the three locations under consideration—Iceland, U.K., and Tropics.

B. Undetected RFI

The difference in the RFI environment for the ascending and descending orbit nodes is explained by considering the antenna pattern projections on the ground for the two orbit nodes, shown in Fig. 5. In the figure, the main lobe is centered at the same spot for both nodes, and the main lobe projection is seen to be very similar in both cases. The projection of the sidelobes differs significantly, and the different RFI environment observed by those sidelobes accounts for the differences in observed RFI.

Our approach to the characterization of the RFI environment, including that of undetected RFI, assumes that low-level RFI entering through the sidelobes can be estimated from detected RFI at other locations, assuming that it entered there through the antenna main beam. This estimator rescales the detected RFI level by the relative antenna gain in the sidelobe and by the relative propagation range from the spacecraft to ground. Since RFI sources are generally point sources rather than extended targets, the RFI contribution from each sidelobe is computed using the Friis transmission formula.

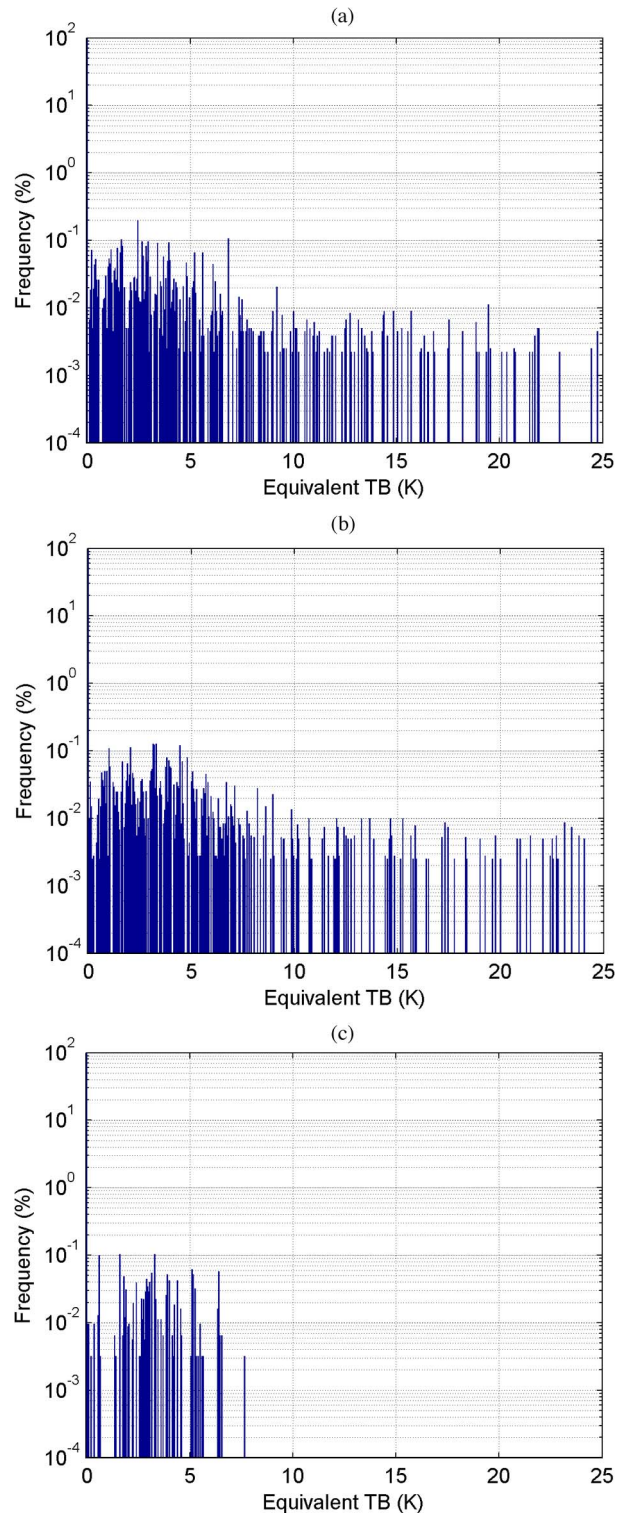


Fig. 4. Ascending node detected RFI distributions for (a) the RFI-rich Iceland location, (b) the medium-RFI U.K. location, and (c) the quiet-RFI Tropics location, with a logarithmic scale on the y -axis. The upper limit of the complete histogram is 3200 K; it is shown in just the 0–25K portion to emphasize the critical low-RFI portion. Note that the x -axis (units of kelvins) denotes the equivalent brightness temperature of the RFI as seen by the instrument.

The RFI detected at a certain location is, in general, composed of sources entering through both the main beam and the sidelobes. A method for isolating these two components was developed in [14] and is applied and expanded upon here. The

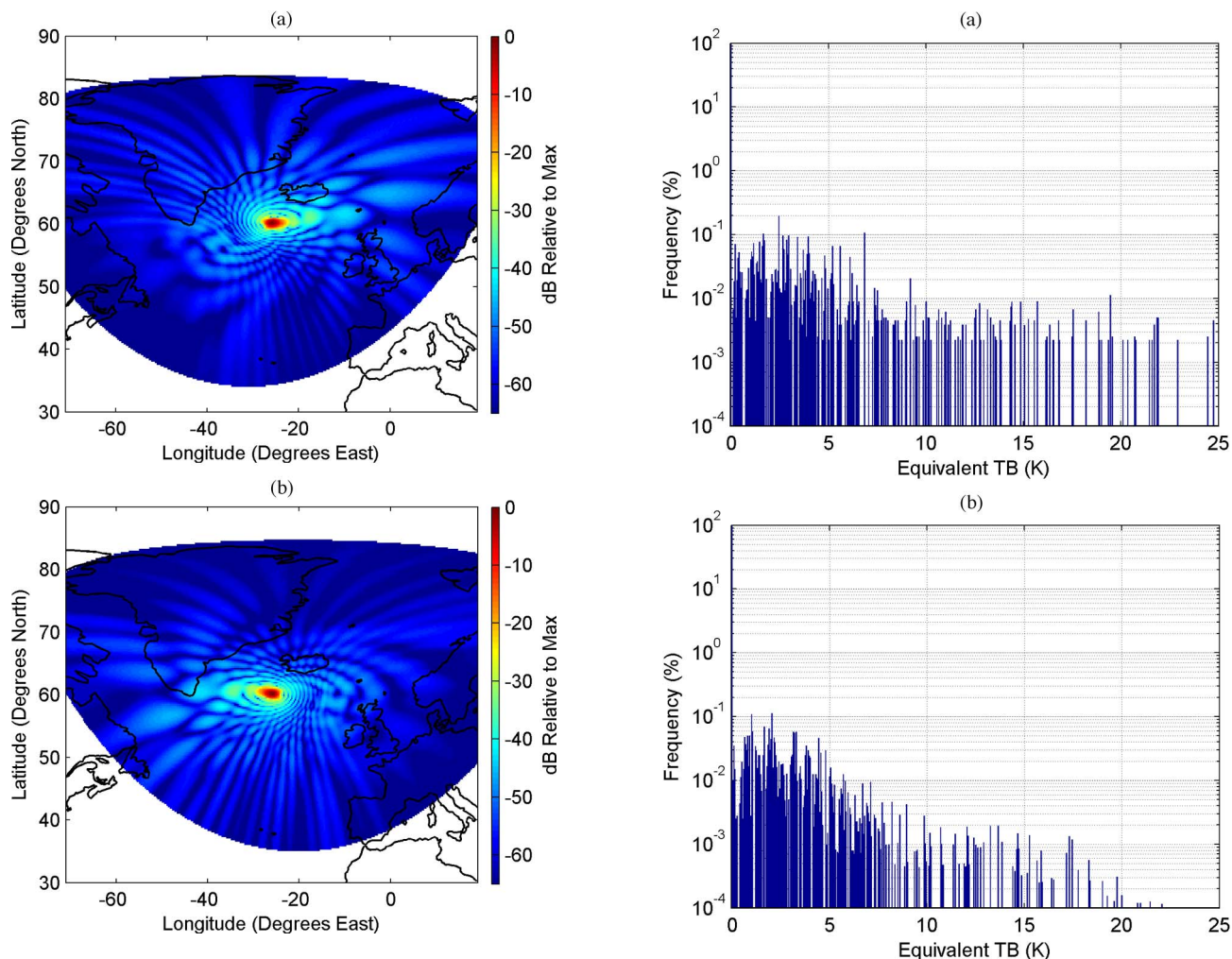


Fig. 5. Ground antenna pattern projection centered at the Iceland location for (a) an ascending pass and (b) a descending pass. These projections include an attenuation factor due to range, as dictated by the Friis transmission formula. The projections are truncated at the horizon.

central hypothesis of the method is that RFI entering through the main beam will, on average, be similar for both ascending and descending orbit nodes since the main beam is pointing at the same location in both cases. (Note that this implicitly assumes that the RFI radiates omnidirectionally from its source.) For RFI entering through the sidelobes, on the other hand, the sidelobes will, in general, be pointing toward very different locations for each orbit node, and the observed RFI will change accordingly. We estimate the RFI entering through the main beam as the portion that is common to both orbit nodes. The resulting main beam-only distributions are shown in Fig. 6. Correction to these distributions due to the nonomnidirectional nature of radiation from actual RFI sources is addressed in the next section.

C. Composite Distribution

The composite RFI distribution at a particular location is composed of contributions from both the main beam and the sidelobes of the antenna pattern boresighted at that location. The contributions from the sidelobes are assembled one at a time from a set of solid angle sectors arranged concentrically

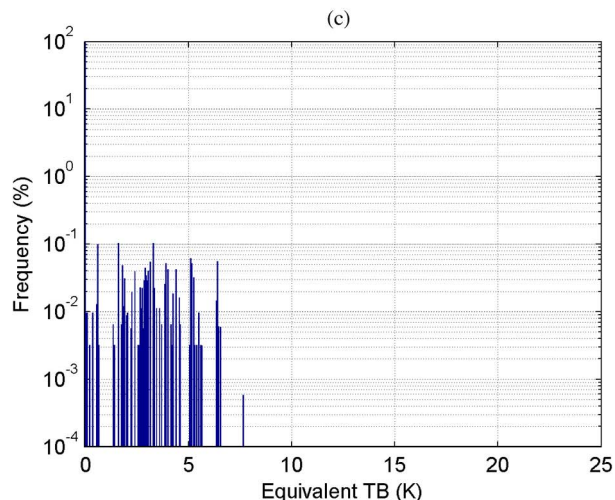


Fig. 6. Ascending node main beam-only RFI distributions for (a) Iceland, (b) U.K., and (c) Tropics.

about the boresight. An example of the antenna pattern and its sectors is shown in Fig. 7.

Note in the figure that the sectors have different areas. High sector density near the boresight is needed to take into account rapidly varying antenna gains, while the density is decreased near the edges to simplify computation. The smallest sector area near the boresight is half of the effective area, and the area

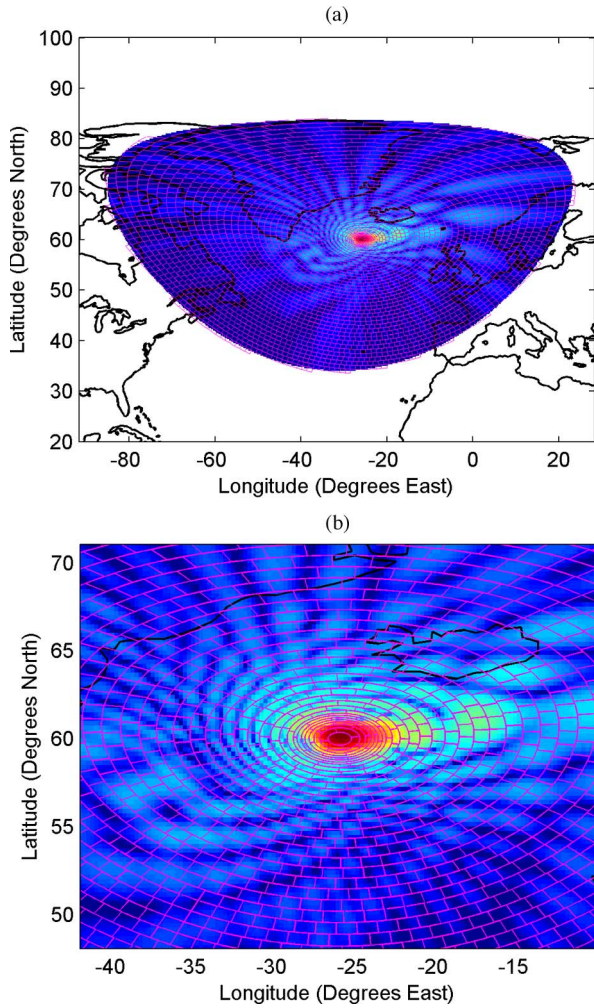


Fig. 7. Sectors used in deriving the composite RFI distribution at the Iceland location: (a) Truncated at the Earth horizon and (b) zoomed in near the antenna boresight.

of the largest sector near the horizon is no more than 2 times the effective area. The effective area for Beam 1 is determined in [14, Section 3] and corresponds to approximately 5.76° in beamwidth, slightly less than the 3-dB beamwidth shown in Table I. The differences in area affect the histograms—they are adjusted accordingly using the method also described in [14, Section 3].

To construct the composite RFI distribution, the main beam-only distributions in each sector of Fig. 7 are weighted by the corresponding antenna gain and range factors, shown in Fig. 5. The weighted contributions from all sectors are then summed. This operation is equivalent to convolving the individual distributions.

One additional correction is made to the composite distribution to account for the possibility that some especially high-level RFI may have been excluded from the main beam-only distribution. This possibility exists because the method used to identify main beam contributions, requiring similar RFI in both ascending and descending node observations, implicitly assumes that the RFI radiates omnidirectionally. Since this may not be the case in practice, some main beam RFI could be omitted from the distribution. To correct for this possibility and

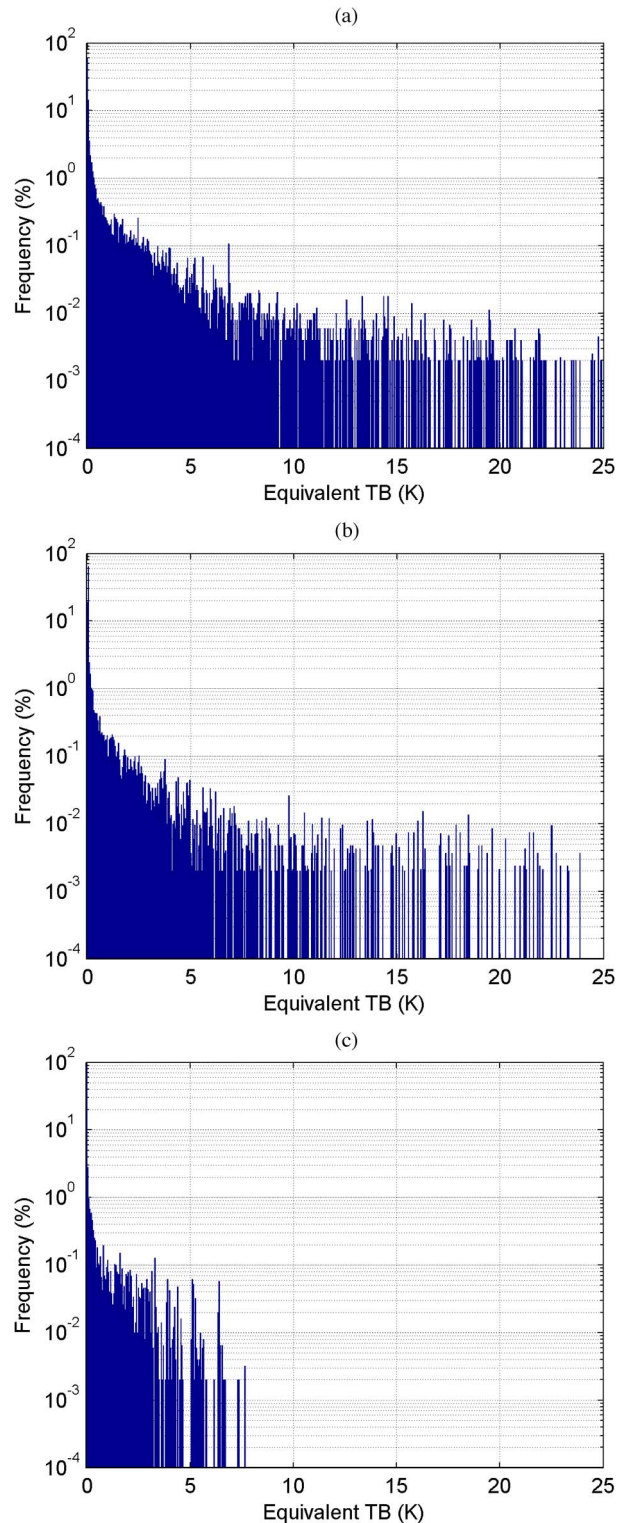


Fig. 8. Ascending node composite RFI distributions for (a) Iceland, (b) the U.K., and (c) Tropics.

add back in the RFI sources that were erroneously excluded, the summed distribution described earlier is compared to the distribution of all detected RFI (both main beam and sidelobe in origin) at the antenna boresight location. At each RFI level, the higher of the two distributions is selected. The resulting distribution is taken as the final composite distribution. Examples are shown in Fig. 8.

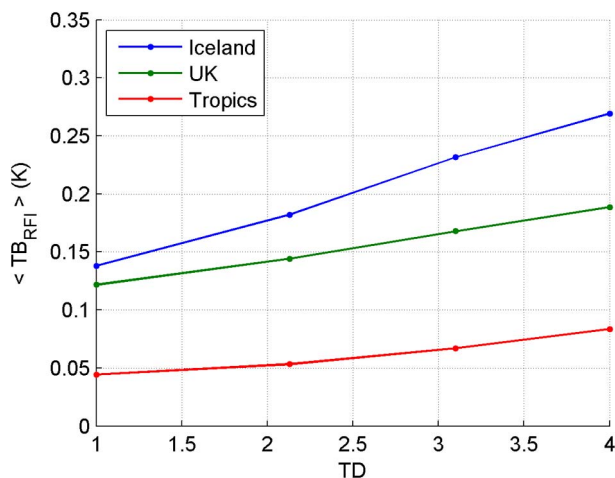


Fig. 9. $\langle TB_{RFI} \rangle$ versus TD for the three representative locations.

The process described earlier for assembling the composite RFI distribution assumes that all of its component distributions are assembled from detected RFI measurements made with common instrument properties. In particular, it assumes that the antenna footprint areas and propagation ranges are all the same. The Aquarius radiometer has three channels, each with its own footprint and range properties. All three channels are needed to completely cover the Earth, so it is necessary to use RFI distributions derived from all three channels. This is done by properly scaling the distributions to account for the differences in footprint area and propagation range. Range effects are corrected by scaling the detected RFI strength of channels 2 and 3 to be consistent with that detected by channel 1. The scale factor is the ratio of the square of the range from each beam to the ground. The differences in footprint size are accounted for by adjusting the RFI distributions for channels 2 and 3 to be consistent with that for channel 1 using the method described in [14, Section 3]. Finally, the three distributions are merged, taking into account the differences in population size of the samples that went into the distributions.

IV. $\langle TB_{RFI} \rangle$ AND MEASUREMENT PRECISION

A. Dependence of $\langle TB_{RFI} \rangle$ on TD

Section III describes how the probability distribution of the effective brightness temperature of RFI is estimated. Section II describes the process by which the RFI distribution, together with the ideal RFI-free Gaussian distribution of brightness temperature, is used to estimate the expected value of the brightness temperature of undetected RFI, denoted as $\langle TB_{RFI} \rangle$. This process is performed at several values of the RFI detection algorithm threshold, TD. Fig. 9 shows the resulting value of $\langle TB_{RFI} \rangle$ as a function of TD for each of the three locations, Iceland, U.K., and Tropics.

As expected, $\langle TB_{RFI} \rangle$ increases monotonically as TD is increased—as the detection threshold is set higher and more tolerant, less RFI is flagged and mitigated, which results in higher levels of undetected RFI. It is also observed for all three locations that the slopes of the $\langle TB_{RFI} \rangle$ versus TD curves tend to increase as TD is increased. Finally and most importantly,

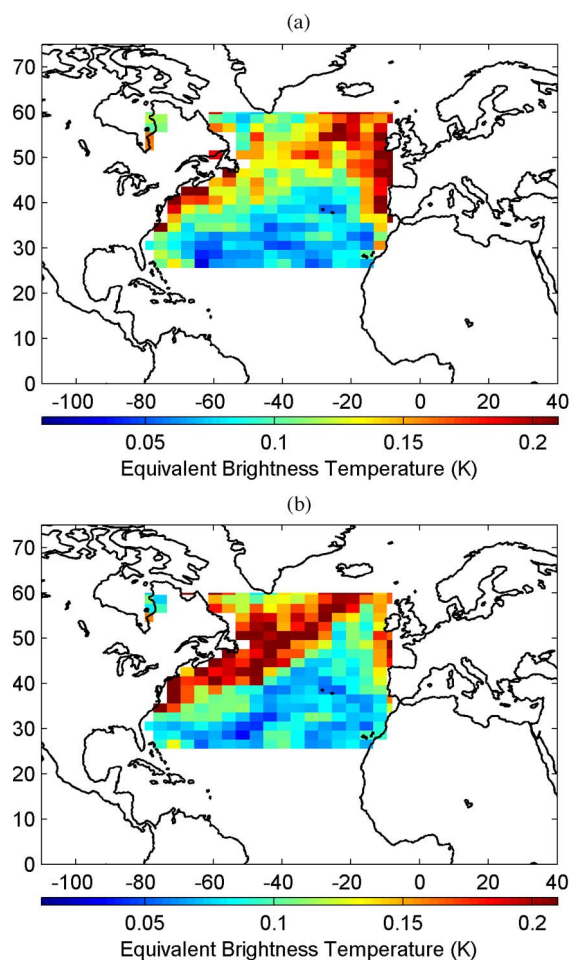


Fig. 10. Expected brightness temperature of undetected RFI for the Aquarius radiometer using a fixed value for the RFI detection threshold, TD, with (a) ascending node and (b) descending node. At each location, $\langle TB_{RFI} \rangle$ versus TD curves like those in Fig. 9 were first generated at four TD values and then interpolated between them to estimate $\langle TB_{RFI} \rangle$ at intermediate values of TD.

note that, for a given value of TD, locations with a higher RFI environment have higher levels of undetected RFI (and hence larger brightness temperature calibration errors).

B. Geographic Variations in $\langle TB_{RFI} \rangle$

Currently, Aquarius uses a constant TD value at all locations. The resulting value of $\langle TB_{RFI} \rangle$, using the Project's current detection threshold value, is shown in Fig. 10 across the North Atlantic region. The result is derived independently for ascending and descending orbit nodes. The most noteworthy feature of the figures is the large variation in undetected RFI brightness with location. Locations nearer the continental land masses tend to have much larger calibration biases due to RFI. Note also the shift in location of the near-land RFI contamination between the two orbit nodes. This is due to the asymmetric angular distribution of the antenna sidelobes about its boresight.

C. Comparison With Geographic- and Node-Dependent SSS Anomaly

Ideally, the SSS retrieved from ascending orbit node data only and that from the descending orbit node data should not

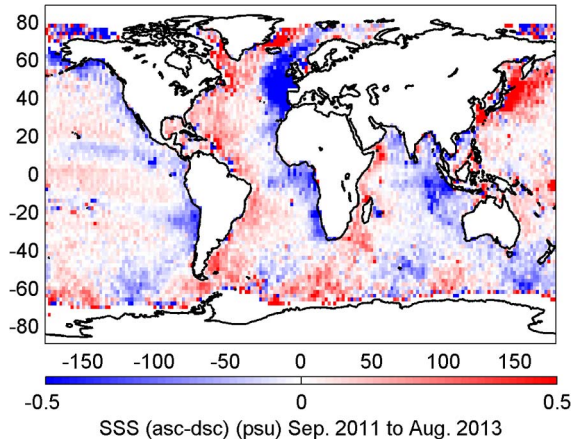


Fig. 11. SSS using ascending node data only minus SSS using descending node data only [18]. Common biases in both ascending and descending orbit nodes do not show up in this map. Significant location-dependent differences are evident.

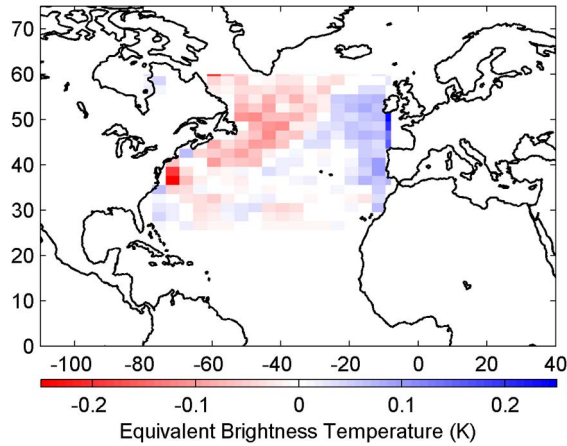


Fig. 12. Ascending minus descending $\langle TB_{RFI} \rangle$.

differ significantly. However, in practice, there is a significant difference, as shown in Fig. 11. The sensitivity of TB to changes in SSS, $(\partial TB / \partial SSS)$, ranges from -0.2 K/psu at an SST of 2°C to -0.7 K/psu at an SST of 33°C . Thus, negative biases in the SSS result from positive biases in TB and vice versa. RFI can only produce positive biases in TB (and negative biases in SSS). Noting that the map is ascending minus descending, the blue regions indicate possible RFI contamination in ascending passes, while the yellow/red regions indicate possible RFI contamination in descending passes.

A similar ascending minus descending map of the undetected RFI brightness temperature is shown in Fig. 12. There is a clear correlation between Figs. 11 and 12, suggesting that undetected RFI is likely contributing to the observed SSS anomaly.

To compare the node-dependent anomalies of SSS and $\langle TB_{RFI} \rangle$ shown in the previous two maps, a scatterplot is shown in Fig. 13. The slope of the least squares line through the points is -0.11 K/psu. The negative slope of the line is consistent with the general dependence of TB on SSS. The magnitude of the slope is much smaller than that for the global average dependence of TB on SSS. It is likely a result of the low SST values that are present where the RFI is most prevalent.

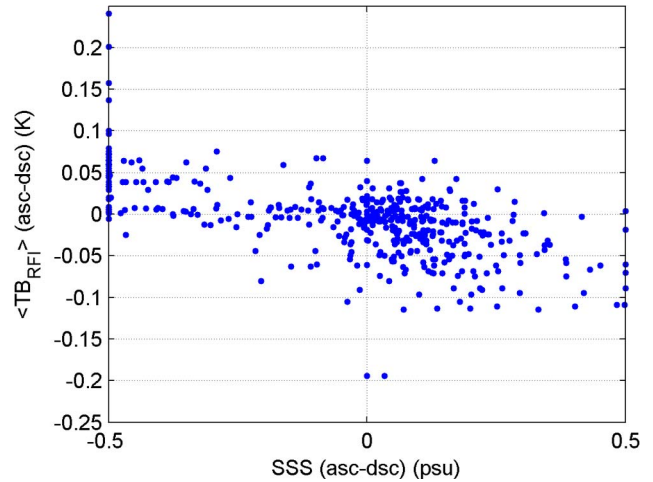


Fig. 13. Node-dependent $\langle TB_{RFI} \rangle$ anomalies versus node-dependent SSS anomalies. A least squares line was derived; its slope is -0.11 K/psu, and the R^2 coefficient of determination is 0.27.

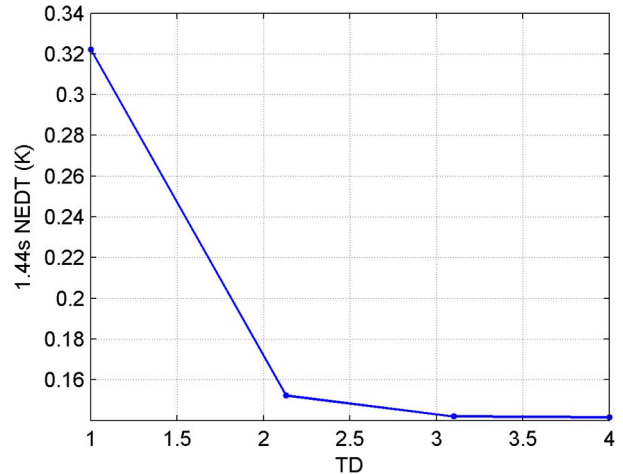


Fig. 14. 1.44-s NEDT versus TD in an RFI-free environment.

D. Dependence of Measurement Precision on RFI Detection Threshold

We now consider the NEDT of the Aquarius 1.44-s data products. In general, the 1.44-s NEDT versus TD relationship depends on the RFI characteristics of the location under consideration. The presence of more RFI in a given location will cause more samples to be discarded for a given TD (which is evident from Step 5 of the RFI algorithm discussed in Appendix A), and the corresponding NEDT will be greater at that location.

For simplicity, when computing the FAR, we consider a scenario with no RFI. Realizations of the thermal emission signal are generated as before and processed with the RFI algorithm. The NEDT is then computed directly as the sample standard deviation of the resulting products. Although this 1.44-s NEDT can be determined theoretically from the NEDT of the 10-ms short accumulations, the Monte Carlo approach is used here because Aquarius uses nonuniform averaging times for the short accumulation samples [11]. The NEDT of the 1.44-s samples is shown in Fig. 14 as a function of TD.

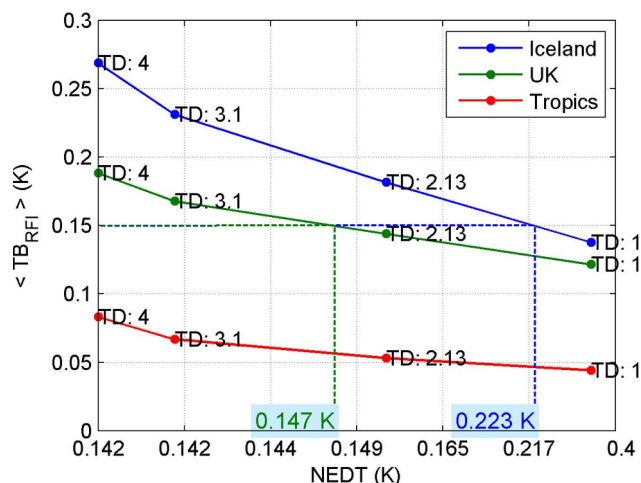


Fig. 15. RROC curve for the three representative locations. Note the nonlinear scale on the x -axis, used to emphasize the dependences. As an example of operating point determination, 0.15 K is chosen in this figure as the desired $\langle TB_{RFI} \rangle$, and the dotted lines show the operating point and resultant NEDT values. Note that the RROC for the Tropics location does not reach 0.15 K for the range of NEDT values shown. A value of $TD > 4$ could, in principle, be chosen in the Tropics location, but there would be only a minor corresponding improvement in NEDT due to the finite sample size being averaged. Large TD values are also undesirable since they increase the likelihood of missed detection of infrequent high-level RFI.

The NEDT of the antenna temperature data product can be seen to decrease monotonically as TD increases—an increase in TD causes less samples to be flagged and discarded, resulting in more samples available to be averaged, decreasing its NEDT.

V. RROC CURVE

The conventional ROC curve illustrates the tradeoff between FAR and PD as a function of detection threshold. In the same sense, a radiometric version of the ROC curve can be created to illustrate the tradeoff between the precision of brightness temperature measurements, as determined by the NEDT, and the calibration accuracy of the measurement, as determined by the expected brightness temperature of undetected RFI or $\langle TB_{RFI} \rangle$. These two radiometer characteristics vary inversely as a function of the RFI detection threshold, TD . Three such “radiometer ROC (RROC)” curves are shown in Fig. 15 for the Aquarius radiometer at the three locations (Iceland, U.K., and Tropics). The values of TD at which the curves are computed are also noted in the figure. Note that the relationship between NEDT and TD for the case of an RFI-free environment shown in Fig. 14 is used here.

Several features are noteworthy in the RROC curves. The consequence of operating with the same value for NEDT at all locations, as is currently done with the Aquarius RFI detection algorithm, can be estimated from the figure by considering a single vertical line at that particular NEDT value. The intersection between the vertical line and the different RROC curves represents the resulting average bias in TB calibration due to undetected RFI at each location. The bias can be seen to vary with location, with higher RFI environments having larger calibration biases. If, on the other hand, a radiometer’s RFI algorithm is adjusted so that the average calibration bias has the same value at all locations, this would be represented in the

RROC curve by a horizontal line at a particular $\langle TB_{RFI} \rangle$ value. This is the scenario shown in Fig. 15, with the calibration bias set at 0.15 K. It is seen that the NEDT is larger in higher RFI environments. In other words, the calibration accuracy could be held constant on average, while the measurement precision is allowed to vary as needed. This would be a more desirable operating condition in cases where accuracy, rather than precision, is a driving performance consideration.

VI. ADAPTIVE TUNING OF THE RFI THRESHOLD TO CONTROL $\langle TB_{RFI} \rangle$

A. Geographic Distribution of TD

As mentioned in Section II, the Aquarius retrieval of SSS is an example of a science objective for which brightness temperature calibration accuracy is a driving requirement relative to measurement precision. In this case, it is desirable to tune the operating point of its RFI detection algorithm, by adjusting TD , so that $\langle TB_{RFI} \rangle$ is held as constant as possible. In practice, it is not possible to force $\langle TB_{RFI} \rangle$ to an arbitrary value due to limiting conditions at both the high and the low end of its dynamic range. $\langle TB_{RFI} \rangle$ will approach an upper bound value as TD becomes arbitrarily large. In that case, no RFI will be detected or mitigated, which is equivalent to not using an RFI algorithm at all. The upper bound on $\langle TB_{RFI} \rangle$ will be the expected value of the equivalent brightness temperature of all RFI present at the given location. On the other hand, the expected value of the clean mean TB may be biased high at some RFI-rich locations (see Appendix A). Since the clean mean does not depend on TD , decreasing TD will not remove this bias. Thus, the lower bound on $\langle TB_{RFI} \rangle$ may be a nonzero positive number. Any value of $\langle TB_{RFI} \rangle$ below this lower bound is thus unattainable.

As an example, we consider a value of 0.1 K as the target for $\langle TB_{RFI} \rangle$. RROC curves like those in Fig. 15 were generated at four TD values for all locations in the North Atlantic region. These RROC curves were then linearly interpolated and extrapolated, as needed, to determine the TD value at each location which corresponds to the target $\langle TB_{RFI} \rangle$. TD values below a practical lower TD limit of 0.1 are set to the lower limit, and the same is done for an upper TD limit of 5. Using any TD value less than 0.1 would cause excessive removal of data, and choosing a TD value that is too high would degrade the algorithm’s ability to detect occasional extremely high RFI signals. The resulting map of TD values across the North Atlantic region considered is shown in Fig. 16.

B. Geographic Distribution of NEDT

Once a TD value is determined for each location, the 1.44-s NEDTs can be estimated from the RROC curve. Using the results from Fig. 14 with an RFI-free approximation, and linear interpolation and extrapolation as needed, the NEDT values corresponding to the TD values shown in Fig. 16 are shown in Fig. 17. Note that, for our target calibration bias of 0.1 K and practical limits on TD , the NEDT varies over the range of ~ 0.15 K to 0.45 K. In many oceanographic applications, this would be considered an acceptable tradeoff between measurement accuracy and precision.

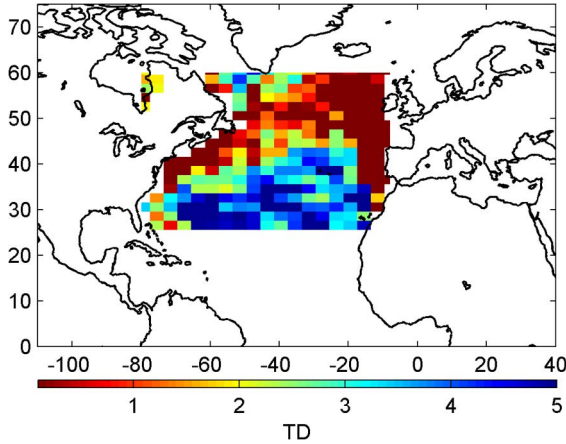


Fig. 16. TD values aimed at equalizing $\langle TB_{RFI} \rangle = 0.1$ K for all locations in the North Atlantic region (for H-Pol and ascending orbit node).

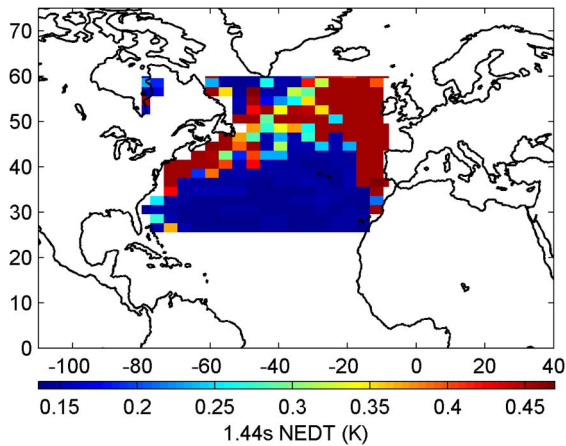


Fig. 17. Resulting 1.44-s NEDTs using the best-effort TDs in Fig. 16.

VII. CONCLUSION

A new procedure has been developed to derive a radiometric version of the ROC curve. It first derives an empirical estimate of the probability distribution of the equivalent brightness temperature of the RFI that is present at a particular location, using detected RFI measurements at that location (for high-level RFI) combined with detected RFI at other locations that is appropriately scaled in magnitude to lower levels. This composite RFI distribution, when combined with a particular RFI detection and mitigation algorithm, allows for the computation of the expected value of the equivalent brightness temperature of the undetected RFI as a function of the detection threshold of the algorithm. This undetected RFI is essentially a calibration bias on the radiometric measurements.

For particular RFI detection algorithm and radiometer instrument properties, it is also possible to compute the FAR of the algorithm. If an RFI mitigation algorithm is used which selectively removes samples with detected RFI, false alarms will have the effect of reducing the number of samples that are available to be averaged together. This reduction in independent samples, in turn, increases the standard deviation of the integrated product. Thus, it is possible to also characterize the pre-

TABLE II
AQUARIUS RFI ALGORITHM PARAMETERS AT LAUNCH [2]

WM	20
WD	5
TM	0.7990
TD	2.1305
Beam 1 H Pol NEDT	0.810 K

cision of the measurement sample as a function of the detection threshold of the RFI algorithm.

When combined together, the variations in calibration bias and measurement precision as a function of the RFI detection threshold constitute an RROC curve. An example of the use of the RROC curve is presented using the Aquarius radiometer. RROC curves are derived at all locations in the North Atlantic region. Using the curves, location-dependent values for the RFI detection threshold are found which result in a roughly consistent average calibration bias across the region. In order to do so, it is necessary to allow the measurement precision to vary as needed. The NEDT is found to vary over the range of ~ 0.15 K to 0.45 K for a target calibration bias of 0.1 K. For ocean surface salinity science applications in which calibration accuracy is a driving concern relative to measurement precision, this would generally be considered an acceptable tradeoff.

APPENDIX A RFI ALGORITHM

The algorithm can be tuned by setting four parameters (see Table II) which are independently adjustable with location [12]:

- 1) WM: local mean running average window size;
- 2) TM: local mean running average glitch threshold;
- 3) TD: RFI detection glitch threshold;
- 4) WD: RFI detection neighborhood/range window size.

The algorithm is applied successively to each 10-ms short accumulation sample. The algorithm to determine if a single sample, called the SUT, should be flagged is follows.

- Step 1: The WM samples surrounding the SUT are identified.
- Step 2: The selected samples from Step 1 are averaged, and this mean is known as the “dirty mean.” Samples whose absolute-valued difference from the dirty mean is greater than TM times the 10-ms NEDT are eliminated. The 10-ms NEDT is currently a fixed number that does not change over time or location.
- Step 3: If there are remaining samples from Step 2, they are averaged to arrive at the “clean mean.” If there are no remaining samples, the clean mean cannot be calculated, and the SUT is flagged.
- Step 4: If the absolute value of the difference between the SUT and the clean mean is greater than TD times the 10-ms NEDT, the SUT is flagged as RFI.
- Step 5: If the SUT is flagged as RFI, WD samples surrounding the SUT are also flagged as RFI as a form of “guard band” surrounding the known RFI. This step is instrumental in flagging contaminated samples whose levels are just below the threshold, due to variations in antenna gain, for example.

TABLE III
MEAN AQUARIUS TA_{SYS} UNDER NOMINAL OCEAN CONDITIONS

	V-Pol	H-Pol
Beam 1	362.0 K	342.7 K
Beam 2	370.8 K	336.3 K
Beam 3	381.7 K	329.4 K

TABLE IV
NOMINAL OCEAN SURFACE CONDITIONS ASSUMED

Quantity	Value
Surface windspeed	10 m/s
Sea surface temperature	15 °C
Sea surface salinity	32 psu
Surface pressure	1013 mbar
Surface absolute humidity	7.5 g/m ³

The current TD is 2.6278; this value is used in Section IV-B to compute the $\langle TB_{RFI} \rangle$ over a region.

Note that the absolute-valued differences in Steps 2 and 4 are needed so that the RFI-mitigated samples have an unbiased expected value in an RFI-free environment.

The clean mean might still be affected by RFI contamination if not all RFI-contaminated samples are removed in Step 2 or if low thermal emission signals are falsely flagged and eliminated (due to a biased dirty mean).

A pulse blanking mitigation algorithm is applied after detection; the RFI-flagged samples are discarded, and the remaining samples are averaged to arrive at the RFI-filtered antenna temperatures, known as TF. The original samples averaged without undergoing RFI mitigation are known as TA. One TF and TA is generated every 1.44 s.

While the fundamental timing unit for Aquarius is 10 ms, 1 ms is reserved for the Aquarius scatterometer transmit pulse, and only 9 ms is available for the radiometer antenna look for every sample. There are $7 * 12 = 84$ 10 – ms radiometry samples every 1.44 s.

APPENDIX B MODELING OF TA_{SYS}

A mean value for TA_{SYS} of 398 K is used in the numerical simulations. It is chosen as follows. The receiver noise temperature of Aquarius is reported as 250 K [11]. Values of $TA_{SYS}(t)$ for each radiometer channel are listed in Table III assuming typical ocean conditions. The surface conditions assumed are tabulated in Table IV. A typical clear-sky plane-parallel atmosphere is assumed. Since Aquarius is primarily an oceanography science mission, we are mainly concerned with TA_{SYS} values over ocean; all tuning locations considered in this paper fall within the ocean (even though RFI sources over land may be detected as well).

The maximum TA_{SYS} occurs over land. If we assume that the maximum land surface temperature is 315 K and the maximum surface emissivity is 1, then the maximum TA_{SYS} will be 565 K. The 398 K value used falls within the dynamic range of natural TA_{SYS} values and is selected a little above its highest ocean value to allow for possible contamination by land as well as RFI. It should be noted that the performance of the Aquarius RFI algorithm is not affected by the value chosen for TA_{SYS} .

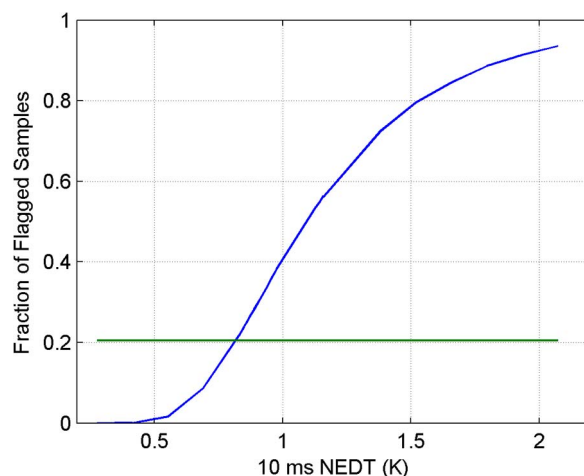


Fig. 18. Determining the 10-ms NEDT of Beam 1 H-Pol. The green line shows the empirically determined FAR. The blue curve depicts FAR as a function of 10-ms NEDT.

APPENDIX C EMPIRICAL ESTIMATION OF THE 10-ms NEDT

The 10-ms sample NEDT is an important characteristic of the Aquarius instrument. Its relevance to this work is twofold. First, the actual thresholds in the RFI algorithm are the product of the TD or TM parameters and the 10-ms NEDT (see Appendix A). Second and more importantly, the 10-ms NEDT is required to model and subsequently generate realizations of $TA_{SYS}(t)$.

Because of the irregular averaging times of the samples required for ground transmission [11], the Allen variance method was not applied here.

The FAR, by definition, is the fraction of RFI-flagged samples over an area with no RFI. Thus, to estimate it, we compute the fraction of flagged samples over an ocean area with as little RFI exposure as possible. The area that we used is bounded by latitudes of 23° south and 2.5° north and longitudes of 137° west and 103° west. This estimated FAR value is shown by the green horizontal line in Fig. 18.

Next, we simulate the FAR in an RFI-free environment as a function of the 10-ms NEDT. As discussed in Section II-A, the thermal emission signal is modeled with a Gaussian distribution. Sequences of thermal emission signals (with no RFI added) are generated with varying 10-ms NEDTs. They are then processed with the same ground-processing code that generated the data used to empirically determine the FAR. From the generated RFI flags, the FAR, or equivalently the fraction of RFI-flagged samples, can then be determined for each NEDT value. The FAR–NEDT relationship is plotted (as the blue curve) in Fig. 18. The 10-ms NEDT that gives the empirical FAR is the desired empirical NEDT.

The NEDT for Beam 1 H-Pol is determined to be about 0.8 K. The actual 10-ms NEDT may be slightly lower due to the estimated FAR (in green) being biased high by the unavoidable presence of low-level RFI.

Strictly speaking, the NEDT depends on the background TB. Thus, as the TB of the location under consideration deviates from the TB of the ocean region mentioned earlier in this section, the NEDT would also shift. In this paper, we considered

tuning at ocean locations only (i.e., when the boresight is pointed at the ocean), and thus, the same NEDT was used to approximate the NEDT at all locations.

ACKNOWLEDGMENT

Data were furnished through the NASA/CONAE Aquarius/SAC-D Project.

The authors would like to thank the following:

- 1) P. de Matthaeis for porting the Aquarius ground-processing code to MATLAB and making it available to the authors;
- 2) E. Dinnat for providing the antenna pattern data and helping with its interpretation and processing;
- 3) T. Meissner for supplying the data for the SSS difference map and for providing a high-resolution land mask;
- 4) S. Brown and other Cal/Val team members for the fruitful telecon discussions;
- 5) F. Patt for assisting with the reading of Aquarius data;
- 6) anonymous reviewers for their careful reading of the manuscript and helpful suggestions.

REFERENCES

- [1] G. S. E. Lagerloef *et al.*, "The Aquarius/SAC-D mission": Designed to meet the salinity remote-sensing challenge," *Oceanography*, vol. 21, no. 1, pp. 68–81, Mar. 2008.
- [2] D. Entekhabi *et al.*, "The Soil Moisture Active Passive (SMAP) mission," *Proc. IEEE*, vol. 98, no. 5, pp. 704–716, May 2010.
- [3] N. Skou, S. Misra, J. E. Balling, S. S. Kristensen, and S. S. Sobjaerg, "L-band RFI as experienced during airborne campaigns in preparation for SMOS," *IEEE Trans. Geosci. Remote Sens.*, vol. 48, no. 3, pp. 1398–1407, Mar. 2010.
- [4] E. Daganzo-Eusebio *et al.*, "SMOS radiometer in the 1400–1427-MHz passive band: Impact of the RFI environment and approach to its mitigation and cancellation," *IEEE Trans. Geosci. Remote Sens.*, vol. 51, no. 10, pp. 4999–5007, Oct. 2013.
- [5] D. McKague, J. J. Puckett, and C. Ruf, "Characterization of K-band radio frequency interference from AMSR-E, WindSat and SSM/I," in *Proc. IEEE IGARSS*, Jul. 25–30, 2010, pp. 2492–2494.
- [6] D. M. Le Vine, "ESTAR experience with RFI at L-band and implications for future passive microwave remote sensing from space," in *Proc. IEEE IGARSS*, Jun. 24–28, 2002, vol. 2, pp. 847–849.
- [7] D. M. Le Vine and M. Haken, "RFI at L-band in synthetic aperture radiometers," in *Proc. IEEE IGARSS*, Jul. 21–25, 2003, vol. 3, pp. 1742–1744.
- [8] S. H. Yueh *et al.*, "Error sources and feasibility for microwave remote sensing of ocean surface salinity," *IEEE Trans. Geosci. Remote Sens.*, vol. 39, no. 5, pp. 1049–1060, May 2001.
- [9] C. S. Ruf, S. M. Gross, and S. Misra, "RFI detection and mitigation for microwave radiometry with an agile digital detector," *IEEE Trans. Geosci. Remote Sens.*, vol. 44, no. 3, pp. 694–706, Mar. 2006.
- [10] R. De Roo, S. Misra, and C. Ruf, "Sensitivity of the kurtosis statistic as a detector of pulsed sinusoidal RFI," *IEEE Trans. Geosci. Remote Sens.*, vol. 45, no. 7, pp. 1938–1946, Jul. 2007.
- [11] D. M. Le Vine, G. S. E. Lagerloef, F. R. Colomb, S. H. Yueh, and F. A. Pellerano, "Aquarius: An instrument to monitor sea surface salinity from space," *IEEE Trans. Geosci. Remote Sens.*, vol. 45, no. 7, pp. 2040–2050, Jul. 2007.
- [12] S. Misra and C. S. Ruf, "Detection of radio-frequency interference for the Aquarius radiometer," *IEEE Trans. Geosci. Remote Sens.*, vol. 46, no. 10, pp. 3123–3128, Oct. 2008.
- [13] S. M. Kay, "Statistical decision theory I," in *Fundamentals of Statistical Signal Processing, Volume II Detection Theory*. Englewood Cliffs, NJ, USA: Prentice-Hall, 1998, sec. 3.4, p. 74.
- [14] D. D. Chen, C. Ruf, "A novel method to estimate the RFI environment," in *Proc. IEEE IGARSS*, Jul. 13–18, 2014, pp. 215–218.
- [15] C. Ruf, D. Chen, D. Le Vine, P. de Matthaeis, and J. Piepmeier, "Aquarius radiometer RFI detection, mitigation and impact assessment," in *Proc. IEEE IGARSS*, Jul. 22–27, 2012, pp. 3312–3315.
- [16] Environ. Modeling Center/National Centers for Environ. Prediction/National Weather Service/NOAA/U.S. Dept. Commerce, "NCEP Climate Forecast System Reanalysis (CFSR) monthly products, January 1979 to December 2010," Res. Data Archive, Nat. Center Atmos. Res., Comput. Inf. Syst. Lab., Boulder, CO, USA, 2010, Accessed on: Sep. 5, 2014. [Online]. Available: <http://rda.ucar.edu/datasets/ds093.2/>
- [17] S. Saha *et al.*, "The NCEP climate forecast system reanalysis," *Bull. Amer. Meteorol. Soc.*, vol. 91, no. 8, pp. 1015–1057, Aug. 2010.
- [18] T. Meissner, F. Wentz, L. Ricciardulli, K. Hilburn, and J. Scott, "The Aquarius salinity retrieval algorithm recent progress and remaining challenges," in *Proc. 13th Spec. Meet. MicroRad Remote Sens. Environ.*, Mar. 24–27, 2014, pp. 49–54.



David D. Chen (S'09) received the Bachelor's degree (with honors) in electrical and computer engineering from the University of Toronto, Toronto, ON, Canada. He is currently working toward the Ph.D. degree at the University of Michigan, Ann Arbor, MI, USA.

His current research interests are in the fields of GNSS-R, ocean wave modeling, and microwave radiometry. He is currently a holder of the NASA Earth and Space Science Fellowship.

Mr. Chen was a recipient of the IEEE Antennas and Propagation Society Predoctoral Research Award in 2012, a fellowship from the Natural Sciences and Engineering Research Council of Canada (NSERC) in 2011, an NSERC Undergraduate Research Award in 2009, and an ECE Department Summer Research Fellowship in 2007.



Christopher S. Ruf (S'85–M'87–SM'92–F'01) received the B.A. degree in physics from Reed College, Portland, OR, USA, and the Ph.D. degree in electrical and computer engineering from the University of Massachusetts at Amherst, MA, USA.

He is currently a Professor of atmospheric and space sciences, a Professor of electrical engineering, and the Director of the Space Physics Research Laboratory at the University of Michigan, Ann Arbor, MI, USA. He has worked previously at Intel Corporation, Hughes Space and Communication, the

NASA Jet Propulsion Laboratory, and Penn State University. His research interests include GNSS-R bistatic scatterometry, microwave radiometry, atmosphere and ocean geophysical retrieval algorithm development, and sensor technology.

Dr. Ruf is a member of the American Geophysical Union, the American Meteorological Society, and the Commission F of the Union Radio Scientifique Internationale. He is a former Editor-in-Chief of the IEEE TRANSACTIONS ON GEOSCIENCE AND REMOTE SENSING and has served on the editorial boards of *Radio Science* and the *Journal of Atmospheric and Oceanic Technology*. He has been the recipient of four NASA Certificates of Recognition and seven NASA Group Achievement Awards, as well as the 1997 TGRS Best Paper Award, the 1999 IEEE Resnik Technical Field Award, the 2006 IGARSS Best Paper Award, and the 2014 GRSS Outstanding Service Award.